

***Final Draft***  
of the original manuscript:

Steglich, D.; Wafai, H.; Brocks, W.:  
**Anisotropic Deformation and Damage in  
Aluminium 2198 T8 Sheets**  
In: International Journal of Damage Mechanics (2009) Sage

DOI: 10.1177/1056789508101916

# **Anisotropic Deformation and Damage in Aluminium 2198 T8 Sheets**

D. Steglich, H. Wafai, W. Brocks

GKSS Research Centre, Institute of Materials Research, Materials Mechanics

D-21502 Geesthacht, Germany

dirk.steglich@gkss.de

**ABSTRACT** – The deformation and damage mechanisms of sheets aluminium alloy 2198 are investigated experimentally and numerically. Mechanical tests in three different orientations are carried out on smooth and U-notched flat specimens. The material's microstructure is characterised to obtain the second phase area content, the morphology of particles and the void volume fraction. The fracture surfaces of the different specimens are examined using scanning electron microscopy. Smooth specimens loaded in the longitudinal and transversal orientation exhibit a slant fracture surface, which has an angle of about  $45^\circ$  with respect to the loading direction. Samples loaded in  $45^\circ$ -orientation fail in a flat manner. Notched specimens show a V-shaped fracture surface. Failure initiates here at the notch root. It is shown that primary voids are first initiated at intermetallic particles. Void growth is promoted and rupture is caused by shear failure between regions of cavities. Finite element calculations are performed to simulate the orientation-dependent deformation and damage behaviour. A phenomenological yield criterion combined with a porosity-based isotropic damage model allows for the quantitative prediction of specimen's failure for different triaxialities. An interaction of deformation and damage evolution can be demonstrated. The deficit of the von Mises yield criterion for this kind of metallic materials becomes evident.

## **1. INTRODUCTION**

Aluminium alloys have been widely used since the early 1900's for structural engineering applications, in transportation industries and in civil engineering. Nowadays, new aluminium alloys are further developed to satisfy the demands of the transportation industries for high strength, improved damage resistance as well as reduction of production cost. Weldable aluminium alloys of 2xxx, 6xxx and 7xxx series have been developed in order to fulfil these requirements. In aerospace industries, 7xxx aluminium alloys are used for plate applications such as wing skin. 6xxx aluminium alloys are applied to thin sheet material application in the fuselage [1]. High strength, good corrosion properties and improved fracture toughness are some of the criteria to be met by newly developed alloys, which come usually with disadvantages like

higher weight or poor fatigue performance. Qualification of a new alloy hence has to cover several aspects. Recently, investigations of mechanical properties, fatigue life, damage tolerance, corrosion resistance and weldability have been carried out [2, 3]. Assessment of residual strength of aircraft structures has been in focus since the launch of NASA's ASIP (Airframe Structural Integrity Program) [4], and several authors have contributed to the development of models, methods and procedures to characterise and predict crack extension in aircraft aluminium alloys, e.g. [5-8]. Characterisation of alloys with respect to resistance against ductile crack extension has become an essential part of a damage-tolerance concept, which acknowledges the existence of cracks and structural damage. However, the R-curve approach of classical fracture mechanics and the respective standards are not suited to describe crack extension in thin sheets and shells, even more as the deformation behaviour of rolled sheets is strongly anisotropic. Damage mechanics provides a unified approach of combining constitutive equations for anisotropic deformation with equations describing the degradation of the material, taking full advantage of the potential of the local approach [9].

The material considered in the present study is a new member of the Al-Cu-Li family, developed in view of applications in aerospace industry. It is a member of the aluminium 2xxx series. These alloys are specifically designed to have good mechanical properties in order to use them for structural components in aircrafts. They have copper (Cu) as major alloying element and hardening is achieved by aging. The new alloy Al 2198 contains also lithium as alloying element to reduce the density and thus to save weight. The chemical composition is given in Table 1. It has superior yield strength than the well established alloy Al 2024, and it is claimed by the producer to have improved damage tolerance, higher corrosion and fatigue resistance, and thermal stability. If proven to be true, this would make the alloy ideal for aircraft fuselage skin and other similar applications [10]. Actual research yields on the optimisation of its damage tolerance, which is of particular relevance for commercial (civil) aircrafts.

This contribution envisages the orientation-dependent deformation under static loading conditions, the failure and damage mechanisms and their prediction by numerical models. Characterisation of the microstructure is made by quantitative image analysis, yielding the morphology of grains and particles in the material. Fractography clarifies the basic mechanisms of failure, which will be modelled using a damage model combined with a description of anisotropic plastic deformation. This material model was realised in the framework of finite elements. The respective parameters are calibrated from tests of smooth and U-notched tensile specimen machined for different orientations of the sheet metal. The generated set of parameters can be used to assess the residual strength of structures with and without flaws, as crack initiation and -extension is included in this type of constitutive model.

## **2. MECHANICAL TESTS**

In order to characterise the alloy's mechanical behaviour, tests have been conducted on three different kinds of specimens, all machined from the same rolled sheet of 3.1 mm thickness:

- Smooth tensile specimens,
- U-notched specimens with notch radius of 1 mm,
- U-notched specimens with notch radius of 2 mm.

Three specimens of each type have been prepared for each of the three directions with respect to the sheet's rolling direction, namely

- along the rolling direction, L “Longitudinal”,
- perpendicular to the rolling direction, T “Transversal”,
- 45° to the rolling direction, D “Diagonal”.

The shape and the dimensions of the tensile specimens are depicted in Fig. 1.

The reported tests were performed under displacement control using a servo hydraulic Zwick 1484 testing machine (maximum force 200 kN) with a constant cross head speed of 0.5 mm/min. Beside the force and elongation, the reduction of width was measured using respective clips in the case of the smooth bars. This allows for a determination of the  $R$ -value (Lankford coefficient)

$$R = \varepsilon_t / \varepsilon_s , \quad (1)$$

where  $\varepsilon_t$  and  $\varepsilon_s$  are strains in transverse and short transversal direction (or thickness direction), respectively. The  $R$ -value provides a more detailed insight in the anisotropic deformation characteristics of the investigated material. It will be used beside the force-elongation signal to calibrate parameters in an anisotropic deformation model. As the displacement in thickness direction  $\varepsilon_s$  is difficult to measure during the tensile tests it was calculated from the two other measured displacements in the longitudinal and transverse direction, assuming constant volume during plastic deformation.

In case of the U-notched specimens, force, elongation and notch opening displacement (NOD) on both notches were recorded providing information on the deformation close to the main studied zone.

## 2.1. Smooth Tensile Specimens

For each orientation at least three specimens have been tested. The scatter between the different test results was negligible. Therefore, one specimen from each direction was selected to represent the respective mechanical behaviour. The results are displayed in Figure 2, showing the applied force,  $F$ , and the reduction of width,  $\Delta w$ , as a function of elongation,  $\Delta L$ .

The three force signals of L, T, and D direction testing are almost parallel. This reveals that strain hardening is the same in all three directions. However, yield stress and tensile strength are highest in L-direction, followed by T and D-direction. While the difference in force at the yielding point is only about 4% between L and T direction, a significant reduction is apparent for D, which is 16%. Hence, the materials response is softer in D-direction, whereas L and T response are quite similar.

Significant differences in the deformation behaviour are also visible from the reduction of specimens' widths, which can be related to the  $R$ -values via the slope of the  $\Delta w$ - $\Delta L$  curve. The width reduction is smallest for the L-direction, resulting in a low  $R$ -value for this orientation. For D being the main loading direction, the observed width reduction is significantly larger, leading to a high  $R$ -value of 2.0. During strain localisation after maximum load the width change is usually not evolving, as necking takes place in thickness direction. The curves for T and D-orientation show an increase of  $\Delta w$  with increasing elongation, however, which results from the formation of a tilted fracture surface. It is interesting to note that macroscopic failure appearance for the three directions differs: for L and T direction the fracture surface is slanted but perpendicular to the loading direction, whereas for D-direction the surface is flat but inclined by  $45^\circ$  to the loading direction. Figure 3 illustrates the different appearances in fracture formation of the smooth bars.

Table 2 summarises the characteristic quantities obtained from the tests on smooth tensile specimens, namely yield stress, tensile strength,  $R$ -value and fracture strain for the three directions tested. All three directions show similar ductilities. The fracture strains lie between 0.13 and 0.16, where the highest value results from the D-direction.

## 2.2. U-Notched Tensile Specimens

Figure 4 displays the results of the tensile tests on U-notched specimens with notch radii of 2 mm and 1 mm, respectively, in terms of macroscopic force and notch opening displacement, NOD. Again, only one representative test result is shown here, as the scatter between the individual tests has been small.

In the case of the moderate notch radius,  $\rho = 2$  mm, the maximum forces obtained in the tests of L and T-direction are identical. The respective difference between the tensile strengths obtained for the smooth bars vanished. This interesting effect is even more pronounced in case of the sharp notch radius,  $\rho = 1$  mm, where the maximum force is achieved in T-direction testing, not in L-direction testing. Obviously the stress triaxiality resulting from the three different specimen geometries affects the maximum load, but this effect is also dependent on the loading direction. An increase in triaxiality induced by the notch sharpness has a stronger influence in T-direction than in L-direction.

The fracture surfaces of the notched specimens are macroscopically V-shaped, with flanges parallel to the specimen's width, oriented  $45^\circ$  to the loading direction. Small regions of flat

crack initiation are visible close to the notch roots. This appearance is independent of the notch radius and the specimen orientation (L, T or D).

### 3. MICROSTRUCTURE

#### 3.1. Grain- and Particle Morphology

Anisotropy of mechanical deformation in metals originates from a direction-dependent spatial distribution of grain orientations, grain shapes and sizes. Whereas orientations of grains can in principle be determined by texture measurements, the sizes and shapes of the grains become visible by polishing and etching plane cross sections of the material. For the aluminium alloy in the current investigation, a Barker's etch has been used to obtain an optimal contrast and visibility of grain boundaries. Pictures have been acquired from three different surfaces using polarised light, having its normal vectors in L, T and S direction, respectively. Figure 5a displays a representative volume with its grain structure, clearly showing the flat shape of the grains with the greatest principal axis in the (LT)-plane. Whereas average grain sizes in L- and T-directions are 20  $\mu\text{m}$  and 10  $\mu\text{m}$ , respectively, the grain dimensions in sheet thickness are reduced due to the rolling process and average only 5  $\mu\text{m}$ . As loading is applied in the sheet plane, the mechanical properties will be primarily influenced by the orientation of the grains, having a size ratio of 2 between L and T direction.

The presence of intermetallic particles, which act as nucleation sites for voids causing ductile damage, determines the damage tolerance of a material. The volume fraction of these particles, their shape and spatial distribution are important microstructural parameters affecting the damage evolution, and hence determine ductility and fracture resistance. The morphology of intermetallic particles can be determined by (2D) microstructural analyses of polished samples and quantified e.g. by its volume content  $A_p$  (ratio of particle area to total area), by the distribution of the mean particle diameters, the shapes of the particles (expressed by the shape factor  $S_f = 4\pi A/U^2$ ,  $A$  being the particles cross section and  $U$  its circumference) and the nearest neighbour distance.

Figure 5b shows the respective representative volume for the particle analysis. Figure 6 reveals that the distributions of the relevant inclusion-related parameters like mean diameter, nearest neighbour distance and shape factor do not depend on the orientation of the investigated cross section. One can therefore assume that inclusions are randomly distributed in space and hence the measured area fractions can be treated as volume fractions of particles,  $f_p$  (see Table 3). For the following modelling approach it can be assumed that second phase particles are isotropically distributed in the material and appear to be almost spherical ( $S_f = 1$ ).

## 3.2. Fractography

Figures 7 to 9 show the fracture surfaces of broken samples of smooth tensile specimen loaded in different directions and of two U-notched specimens loaded in L-direction investigated by scanning electron microscopy. The first set of fractographs (Fig. 7) is taken from the slanted surface of the L-loaded specimen. Large regions of flat grains can be found (left part of the figure), revealing a shear mechanism leading to failure. However, at larger magnification, isolated regions covered with dimples appear. These regions are very small, but they indicate that at least the initiation of failure is governed by void nucleation and growth. Similar findings can be obtained from fracture surfaces of smooth specimens loaded in T-direction (not shown here). The fraction of regions showing dimples however appears to be slightly higher.

The situation is different for D-loaded specimen. As already pointed out, the macroscopic appearance of the fracture surface is flat, but inclined with respect to the loading direction. The rupture surface itself shows large regions of dimples, the larger ones including second phase particles, see figure 8. The formation of dimples around particles of about 2-5  $\mu\text{m}$  gives clear evidence that damage has initiated by debonding of particles from the surrounding matrix, which have been identified by the microstructural investigations. The presence of smaller voids between the large particles indicates that after a void growth phase the coalescence mechanism is governed by intervoid linking.

In case of the notched specimens tested, different regions on the fracture surfaces can be identified by SEM pictures. In regions close to the notch root, the above mentioned dimples indicating a ductile damage mechanism can be found. In the middle part of the specimens, on the V-shaped surfaces, flat regions dominate, which originate from inter-crystalline shear fracture. Figure 9 shows the two regions of the fracture surface of a notched specimen ( $\rho=1\text{ mm}$ ), showing the notch root region (left) and the specimen's middle (right). This particular specimen was loaded in D-direction, but the same characteristics can be also found in the respective test in L- and T-direction.

All in all this implies that modelling of damage evolution, crack initiation and extension should be based on porous metal plasticity, although a second mechanism (shear failure) is present at low triaxialities in L- and T-direction.

## 4. MODELLING OF DEFORMATION AND DAMAGE

### 4.1. Constitutive Model

The constitutive model described below is based on an anisotropic yield surface according to Bron and Besson [11] incorporating the effect of hydrostatic pressure on the growth of microvoids. Hardening and damage evolution are assumed as isotropic. The model has been successful in capturing deformation and fracture of Al 2024 and is expected to be capable of modelling the behaviour of the new alloy Al 2198 as well. The classical theory of plasticity will be shortly reviewed to explain the notation and the concept behind Bron's model. With regard to

the description of anisotropic yielding, a Voigt notation is used for all tensors in the following. The second order symmetric stress tensor is represented by a six-component vector,

$$\begin{aligned}\underline{\sigma}^T &= (\sigma_i) = (\sigma_1 \ \sigma_2 \ \sigma_3 \ \sigma_4 \ \sigma_5 \ \sigma_6) \\ &= (\sigma_{11} \ \sigma_{22} \ \sigma_{33} \ \sqrt{2}\sigma_{12} \ \sqrt{2}\sigma_{23} \ \sqrt{2}\sigma_{31})\end{aligned}\quad (2)$$

As in the classical theory of incremental, rate-independent plasticity, yielding is modelled by a convex yield surface, which encloses all stress states causing elastic deformations and expands isotropically during plastic deformation. The yield condition is written as

$$\varphi(\underline{\sigma}, \underline{\epsilon}^p) = \bar{\sigma} - R(p) = 0, \quad (3)$$

where  $\bar{\sigma}$  is an appropriately defined equivalent stress,  $R(p)$  the current flow stress, and  $p$  the associated accumulated equivalent plastic strain. As the hydrostatic stress, i.e. the first invariant of the stress tensor,

$$\sigma_h = \frac{1}{3} \sum_{k=1}^3 \sigma_k, \quad (4)$$

does not affect plastic yielding, the yield surface is described by the deviatoric stresses

$$\sigma'_i = \begin{cases} \sigma_i - \sigma_h & i = 1, 2, 3 \\ \sigma_i & i = 4, 5, 6 \end{cases} \quad (5)$$

Isotropic behaviour requires that the equivalent stress,  $\bar{\sigma}$ , depends on the stress invariants, only. If any effect of the third invariant is neglected, the von Mises yield condition with

$$\bar{\sigma}_{\text{Mises}} = \sqrt{\frac{3}{2} \underline{\sigma}' \cdot \underline{\sigma}'} = \sqrt{\frac{3}{2} \sigma'_i \sigma'_i} \quad (6)$$

is obtained. The associated equivalent plastic strain rate has to satisfy the equivalence condition for the work of plastic dissipation

$$\bar{\sigma} \dot{p} = \underline{\sigma} \cdot \dot{\underline{\epsilon}}^p. \quad (7)$$

The von Mises equivalent stress, eq. (6), yields

$$\dot{p} = \sqrt{\frac{2}{3} \dot{\underline{\epsilon}}^p \cdot \dot{\underline{\epsilon}}^p} = \sqrt{\frac{2}{3} \dot{\epsilon}_i^p \dot{\epsilon}_i^p}. \quad (8)$$

The plastic strain rates result from the associated flow rule or normality rule stating that they are normal to the yield surface,

$$\dot{\underline{\epsilon}}^p = \dot{p} \frac{\partial \varphi}{\partial \underline{\sigma}} = \dot{p} \frac{\partial \bar{\sigma}}{\partial \underline{\sigma}}. \quad (9)$$

The von Mises yield surface is isotropic. The first anisotropic yield function for rolled sheets exhibiting orthotropy has been introduced by Hill [12] by inserting six parameters  $h_i$  into the von Mises definition of the effective stress,

$$\bar{\sigma}_{\text{Hill}} = \sqrt{\frac{3}{2} \sum_{i=1}^6 h_i \sigma'_i \sigma'_i} . \quad (10)$$

A generalised isotropic yield surface, which allows for arbitrary intermediate shapes between the von Mises and the Tresca yield function, has been proposed by Hosford [13],

$$\bar{\sigma}_{\text{Hosford}} = \left( \frac{1}{2} \left( |\sigma'_I - \sigma'_{II}|^a + |\sigma'_{II} - \sigma'_{III}|^a + |\sigma'_{III} - \sigma'_I|^a \right) \right)^{1/a} , \quad (11)$$

where  $\sigma'_I$ ,  $\sigma'_{II}$ ,  $\sigma'_{III}$  are the principal deviatoric stresses. Barlat et al. [14] extended this yield function to orthotropic materials by introducing a modified stress deviator,

$$\underline{\mathbf{s}}' = \underline{\mathbf{L}} \cdot \underline{\boldsymbol{\sigma}}' . \quad (12)$$

$\underline{\mathbf{L}} = (L_{ij})$  is a fourth order tensor written as a 6×6 matrix in the Voigt notation, which contains 6 material constants,  $c_1$  to  $c_6$ , describing the anisotropy. Finally, Bron and Besson [11] defined an equivalent stress

$$\bar{\sigma} = \left[ \alpha \bar{\sigma}_1^a + (1 - \alpha) \bar{\sigma}_2^a \right]^{1/a} , \quad (13)$$

by the superposition of two functions

$$\bar{\sigma}_1 = \left[ \frac{1}{2} \left[ \left| s_1^{r(1)} - s_{II}^{r(1)} \right|^{b_1} + \left| s_{II}^{r(1)} - s_{III}^{r(1)} \right|^{b_1} + \left| s_{III}^{r(1)} - s_1^{r(1)} \right|^{b_1} \right] \right]^{1/b_1} , \quad (14)$$

$$\bar{\sigma}_2 = \left[ \frac{3^{b_2}}{2^{b_2} + 2} \left( \left| s_1^{r(2)} \right|^{b_2} + \left| s_{II}^{r(2)} \right|^{b_2} + \left| s_{III}^{r(2)} \right|^{b_2} \right) \right]^{1/b_2} ,$$

where  $s_1^{r(k)}$ ,  $s_{II}^{r(k)}$ ,  $s_{III}^{r(k)}$  ( $k = 1, 2$ ) are the principal values of two modified stress deviators defined as

$$\underline{\mathbf{s}}^{r(k)} = \underline{\mathbf{L}}^{(k)} \cdot \underline{\boldsymbol{\sigma}}^{r(k)} , \quad (15)$$

with

$$\underline{\underline{\mathbf{L}}}^{(k)} = (L_{ij}^{(k)}) = \begin{pmatrix} (c_2^{(k)} + c_3^{(k)})/3 & -c_3^{(k)}/3 & -c_2^{(k)}/3 & 0 & 0 & 0 \\ -c_3^{(k)}/3 & (c_3^{(k)} + c_1^{(k)})/3 & -c_1^{(k)}/3 & 0 & 0 & 0 \\ -c_2^{(k)}/3 & -c_1^{(k)}/3 & (c_1^{(k)} + c_2^{(k)})/3 & 0 & 0 & 0 \\ 0 & 0 & 0 & c_4^{(k)} & 0 & 0 \\ 0 & 0 & 0 & 0 & c_5^{(k)} & 0 \\ 0 & 0 & 0 & 0 & 0 & c_6^{(k)} \end{pmatrix}. \quad (16)$$

The four material parameters  $a$ ,  $b_1$ ,  $b_2$ ,  $\alpha$ , affect the shape of the yield surface as in Hosford's model, eq. (11), but not its anisotropy, which is controlled by the 12 constants  $c_i^{(k)}$ ,  $k = 1, 2$ ,  $i = 1, \dots, 6$ . Altogether, the yield function contains 16 parameters. To ensure convexity and differentiability,  $a \geq 1$  and  $b_k \geq 2$  is required as Bron and Besson [11] showed. In the case of  $c_i^{(1)} = c_i^{(2)}$  and  $a = b_1 = b_2$ , Bron's yield function corresponds to that of Karafillis and Boyce [15], and for  $\alpha = 1$  to the yield function of Barlat et al. [14]. The yield function of von Mises, eq. (6), is obtained for  $\alpha = 1$  and  $c_i = 1$  if  $a = 2$  or 4, and that of Tresca if  $a = 1$  or  $+\infty$ . The effects of the various parameters on the shape of the yield surface is discussed in detail in the paper of Bron and Besson [11]. It turns out, that particularly the transition from a Mises-type to a Tresca-type yield surface is essential to meet the experimentally observed phenomena as described in section 2.

The effective strain rate,  $\dot{p}$ , is obtained from eq. (7), and normality of the plastic strain rates as in eq. (9) is postulated again. Though the yield surface is anisotropic, hardening is isotropic, as it depends on the scalar variable  $p$ , only.

Damage of the material results in softening and requires the incorporation of the hydrostatic stress, eq. (4), into the yield function. The most common model for isotropic damage in ductile materials is the GTN model named after Gurson [16], Tvergaard and Needleman [17], who proposed a yield surface described by

$$\frac{\bar{\sigma}^2}{R^2(p)} + 2q_1 f^* \cosh\left(q_2 \frac{3\sigma_h}{2R(p)}\right) - 1 - (q_1 f^*)^2 = 0. \quad (17)$$

$f^*$  is a scalar internal variable of damage related to the void volume fraction or porosity,  $f$ , and  $q_1$ ,  $q_2$  are additional material parameters. The porosity develops by two contributions, namely by void nucleation and void growth,

$$\dot{f} = \dot{f}_{nuc} + \dot{f}_{growth}. \quad (18)$$

For the nucleation term a constant nucleation rate starting at a threshold value of the plastic equivalent strain is considered here,

$$\dot{f}_{nuc} = A H(p - \varepsilon_0), \quad (19)$$

with  $H$  being the Heaviside function and  $A$  and  $\varepsilon_0$  model parameters. This particular non-saturating nucleation function has been chosen to support void growth at high plastic strains on a phenomenological basis.

Void growth evolves following

$$\dot{f}_{growth} = (1-f) \sum_{k=1}^3 \dot{\varepsilon}_k^p = (1-f) \dot{\varepsilon}_{vol}^p, \quad (20)$$

starting from an initial porosity  $f_0$ . Different from undamaged materials, the plastic volume dilatation rate,  $\dot{\varepsilon}_{vol}^p$ , in porous materials is not zero.

The mathematical model as described above has been realised in the object-oriented FE code Zébulon [18]. It has been linked via the material library Z-mat to the commercial finite element program ABAQUS/Standard, which is used to perform the simulations in the present contribution. A similar framework has been applied by Bron et al. [19] using the damage model of Rousselier [20] instead of the GTN model as in the present contribution.

## 4.2. FE models

Despite the fact that the specimen thickness is comparably small, 3D discretisation is used for the simulations. As shown in [21], the stress triaxiality in plane stress elements is too low to activate void growth. As a consequence, crack formation will be underestimated if plane stress conditions are prescribed. Due to symmetry of the specimen geometry and the orthotropy of the material one eighth of the specimens is modelled, exploiting the threefold symmetry of the problem. A coarse mesh is used for the specimens except for regions of stress concentration and necking. In these regions the mesh has been refined to allow good simulation of necking and constraints caused by the notches. Figure 10 shows the centre regions of the smooth bar and the U-notched samples with  $\rho = 1$  mm and  $\rho = 1$  mm. Quadratic elements (3D bricks with 20 nodes) have been used for discretisation. Three elements are used over the half thickness. A typical dimension of a finite element is 0.2 mm in main loading and width directions and 0.51 mm in thickness direction in case of the smooth bar. For the U-notched specimens, the size of the finite elements at the notch root was 0.17 mm in loading and width direction.

The specimens were loaded under displacement control with a prescribed linear amplitude function. Finite strains are accounted for. The material's anisotropy is realised via local coordinates, each assigned to one of the considered loading directions.

## 4.3. Parameter Identification Strategy

The determination of the model parameters is split into five tasks, following a step-by-step procedure similar to the one proposed by Bron and Besson [11]. The objective is to find one set of parameters that can reproduce the experiments.

Identification was then performed as follows:

1. Assuming isotropic elasticity and using the elastic constants ( $E, \nu$ ) from similar alloys,
2. Assuming identical work hardening behaviour for all directions and determination of isotropic plastic hardening  $\sigma(\varepsilon^p)$  from L-direction as a reference from the respective tensile test of a smooth specimen,
3. Determination of the parameters  $\alpha, a, b_1, b_2$  affecting the shape of the yield surface by considering smooth and notched specimens loaded in L-direction,
4. Adjustment of anisotropy parameters  $c_i^{(k)}$  by considering all specimen geometries and load directions,
5. Calibration of damage parameters from microstructural investigations and comparison of the respective simulation with the force-elongation record of notched specimens.

It is worth remembering that in steps 3 and 4 in total 12 experimental curves have to be taken into account simultaneously: 9 force vs. elongation curves for the three tensile specimens in three directions as well as the  $R$ -values of the smooth bars in the three directions.

The elastic constants have been selected to be  $E = 73000$  MPa and  $\nu = 0.33$ . The hardening function in terms of true stress and true (logarithmic) plastic strain was taken from the test in L-direction up to the load maximum and extrapolated using a power-law function

$$\sigma = 468 \text{ [MPa]} (1 + 40.95\varepsilon^p)^{0.1202}. \quad (21)$$

The next step requires the determination of the yield surface parameters  $\alpha, a, b_1, b_2$ . In a first attempt  $\alpha$  was set to one, as it gave the best fit for the notched geometries in longitudinal direction. Setting  $\alpha = 1$  corresponds to the early Barlat (1991) model [14]. Parameters  $a, b_2$  become irrelevant, and only  $b_1$  should be fit. Since the second sub-function  $\bar{\sigma}_2$  is not accounted for, parameters  $c_i^{(2)}$  also become irrelevant.  $b_1$  was set to 20 and the first attempt to fit anisotropy parameters was done. However it was not possible to fit force vs. elongation curves and Lankford coefficients at the same time.

After that  $\alpha$  was set to a value less than 1, which means that the full capacity of anisotropy parameters was used. Finally the isotropy parameters were set to the following values:

$$\alpha = 0.5; \quad a = b_1 = b_2 = 16. \quad (22)$$

An important limitation for the exponents  $b_1$  and  $b_2$  is  $b_1, b_2 \leq 20$ . The higher their values, the sharper the edges of the yield surface are, until the yield surface finally becomes similar to Trescas yield surface in the case of  $b_1, b_2 \rightarrow \infty$ . For values higher than 20, the simulation might fail due to convergence problems rising from the presence of vertices in the surface and the non-unique normal vector.

The model contains 12 anisotropy parameters, but for the case of thin sheets usually a plane stress state is considered. Thus the last two parameters of each modified stress tensor will not be changed since the respective components are related to the thickness direction,  $c_{i=5,6}^{(k)} = 1$ . After performing comprehensive parametric studies, a set of anisotropy parameters was chosen that yields to a good fit of all individual target functions. The coefficients of this set are summarised in Table 4. Unfortunately, the  $R$ -value of the smooth specimen in the transversal direction could not be met by the simulations – it has always been underestimated by about 20%. The determination of the yield surface and anisotropy parameters was carried out without considering damage. This is possible because the particle – and thus void – volume fraction was small. Damage evolution only affects the global specimen behaviour in the final state of deformation prior to failure.

The particle surface fraction ( $A_p=0.0027$ ) obtained from the microstructural analysis (LT-plane) was then taken as an initial volume fraction for the damage model,  $f_0$ . From the macroscopic force-NOD curves it became clear that an additional void nucleation function had to be used and that the void growth phase prior to coalescence had to be rather small. Thus, a constant void nucleation rate of 0.02 controlled by the equivalent plastic strain higher than the threshold value of 0.1 is introduced and the value of the critical void volume fraction was set to 0.009. The remaining parameters of the damage model are given in Table 4.

## 5. SIMULATION RESULTS

For comparison and particularly for showing the inadequacy of a yield surface of the Mises type, the simulations of the tests in L-direction applying von Mises equivalent stress, eq. (6), will be included in the following graphs. Though Hill's equivalent stress, eq. (11), accounts for anisotropy, the yield surface is actually of the same type. Hence, without showing the respective results, it was found that the simulations were not able to fit the experimental data. This can be easily concluded from the performance of the von Mises yield condition.

Figure 11 shows a comparison between simulation and test results in terms of the applied force,  $F$ , and the reduction of width,  $\Delta w$ , as a function of elongation,  $\Delta L$ , for the smooth tensile bars of L-, T- and D-orientation. Damage evolution has been considered in the simulations. The force vs elongation curves of tests and simulations agree quite well. The test in L-direction is additionally simulated applying von Mises equivalent stress and without accounting for damage evolution. Certainly, the deformation of a smooth specimen in uniaxial tension can be described by the yield condition of von Mises, and so the two other orientations could have been simulated taking the different yield curves into account. The crucial deficit however is the performance under varying triaxiality, as the simulations of the notched tensile bars will show (see Figure 12).

Figure 11 also contains the results of the width reduction,  $\Delta w$ , in dependence on  $\Delta L$ . The coincidence between experimental and numerical results for  $\Delta L \leq 4.5$  mm is good, except for the T-orientation. No explanation could be found for the significant deviation of the latter. The simulations predict localisation of deformation in thickness reduction, which results in a

constant  $\Delta w$ , starting at an elongation of 4.5 to 5 mm for all orientations, which has not been observed in the tests of T- and D-orientations. At least for the D-orientation the steep increase of  $\Delta w$  may be an artefact produced by the clip gauges and the 45° inclined fracture formation, however, as has been discussed in section 2.1 already.

The constitutive model was now applied to the notched specimens using the same set of parameters for anisotropic deformation including damage evolution. The results are displayed in Figure 12. The simulations based on von Mises' yield condition do not meet the tests results for the L-orientation at all, though they fitted to the respective results of the smooth specimen, i.e. for a predominantly uniaxial stress state, see Figure 11. This indicates that the elliptical shape of the yield surface is not suited to describe biaxial stress states. The Bron model with the yield surface shown in Figure 13 meets the test results for both notch radii,  $\rho = 2$  mm (left) and  $\rho = 1$  mm (right), quite well, and failure is also predicted satisfactorily, except for the D-orientation and the sharp notch,  $\rho = 1$  mm. Remarkably, the model of isotropic damage predicts different notch-opening displacements at fracture in dependence on the orientation. The deformation anisotropy obviously affects the nucleation term of eq. (19).

## 6. CONCLUSIONS

Though Hill's yield condition accounts for anisotropy, the elliptical shape of the yield surface is its essential deficit making it unsuited for describing triaxial stress states in aluminium alloys. The ability of Hosford's and Bron's model to represent various shapes of yield surfaces between the von Mises ellipse and the Tresca hexagon in dependence on the  $a$ -parameter is the reason for their good performance.

The orientation-dependent deformation of an advanced aluminium alloy and its failure under static loading could be successfully simulated with a constitutive model of anisotropic plasticity proposed by Bron and Besson in combination with the GTN model of isotropic damage evolution. The numerous material parameters were identified by fitting the simulation results to the respective test data. Supporting information has been obtained from microstructural analyses and fractography.

The microstructural analyses indicated that the deformation anisotropy in the sheet plane is due to the different grain orientations in L and T direction. The second phase particles were approximately randomly distributed and of almost spherical shape, however, so that damage could be modelled as isotropic. The deformation anisotropy nevertheless induced orientation dependent failure.

The V-shaped fracture surface ("roofing") observed for the notched specimens is beyond the scope of the present models. This phenomenon has also been observed in centre-cracked panels tested with anti-buckling devices which prevented slant fracture [22] and is obviously induced by geometrical constraints. It should also be emphasised that assuming isotropic damage for the modelling of rolled aluminium sheet is a rough approach, at least from the micromechanical point of view. Several authors have reported that in rolled sheet particles are aligned in chains,

and the special distribution of these chains is not isotropic, e.g. [23]. Accounting for damage anisotropy becomes a challenging task [24, 25], which requires higher effort in constitutive formulations, mechanism- and parameter identification.

## 7. Acknowledgements

The authors would like to thank their colleagues from GKSS research centre for their contributions: K. Erdmann for conducting the mechanical tests, V. Ventzke for performing the SEM investigations, and P. Fischer for preparing the microstructure graphs.

## 8. Literature

- [1] Ehrström J, Warner T. Metallurgical design of alloys for aerospace structures. *Mater Sci Forum*. 2000;331-337:5-16.
- [2] Heinz A, Haszler A, Keidel C, Moldenhauer S, Benedictus R, Miller WS. Recent development in aluminium alloys for aerospace applications. *Mater Sci Eng A*. 2000;280(1):102-107.
- [3] Liu J, Kulak M. A new paradigm in the design of aluminium alloys for aerospace applications. *Mater Sci Forum*. 2000;331-337:127-140.
- [4] Harris. Structural integrity of aging airplanes. In: Atluri SN, editor. *International Symposium on Structural Integrity of Aging Airplanes*. Atlanta: Springer; 1990. p. 141-152.
- [5] Nègre P, Steglich D, Brocks W. Crack extension in aluminium welds: a numerical approach using the Gurson-Tvergaard-Needleman model. *Eng Fract Mech*. 2004;71(16-17):2365-2383.
- [6] Roychowdhury S, Roy YDA, Dodds Jr. RH. Ductile tearing in thin aluminum panels: experiments and analyses using large-displacement, 3-D surface cohesive elements. *Eng Fract Mech*. 2002;69:983-1002.
- [7] Newman Jr. JC, James MA, Zerbst U. A review of the CTOA/CTOD fracture criterion. *Eng Fract Mech*. 2003;70:371-385.
- [8] Roy YDA, Dodds Jr. RH. Simulation of ductile crack growth in thin aluminum panels using 3-D surface cohesive elements. *Int J Fract*. 2001;110:21-45.
- [9] Lemaitre J. Local approach of fracture. *Eng Fract Mech*. 1986;25(5/6):523-527.
- [10] Warner T. Recently-developed aluminium solutions for aerospace applications. *Materials Science Forum*. 2006;519-521:1271-1278.
- [11] Bron F, Besson J. A yield function for anisotropic materials: Application to aluminium alloys. *Int J Plast*. 2004;20(4-5):937-963.
- [12] Hill R. A theory of the yielding and plastic flow of anisotropic metals. *Proc Roy Soc London A*. 1948;193:281-297.
- [13] Hosford WF. Generalized isotropic Yield Criterion. *Journal of Applied Mechanics*. 1972;39(2):607-&.

- [14] Barlat F, Lege DJ, Brem JC. A six-component yield function for anisotropic materials. *International Journal of Plasticity*. 1991;7(7):693-712.
- [15] Karafillis AP, Boyce MC. A general anisotropic yield criterion using bounds and a transformation weighting tensor. *Journal of the Mechanics and Physics of Solids*. 1993;41(12):1859-1886.
- [16] Gurson AL. Continuum theory of ductile rupture by void nucleation and growth: part I - yield criteria and flow rules for porous ductile media. *J Eng Mater Technol-Trans ASME*. 1977;99:2-15.
- [17] Tvergaard V, Needleman A. Analysis of the cup-cone fracture in a round tensile bar. *Acta Metall*. 1984;32(1):157-169.
- [18] Besson J, Foerch R. Large scale object-oriented finite element code design. *Computer Methods in Applied Mechanics and Engineering*. 1997;142(1-2):165-187.
- [19] Bron F, Besson J. Simulation of the ductile tearing for two grades of 2024 aluminum alloy thin sheets. *Eng Fract Mech*. 2006;73(11):1531-1552.
- [20] Rousselier G. Ductile fracture models and their potential in local approach of fracture. *Nucl Eng Des*. 1987;105:97-111.
- [21] Sun D-Z, Hömig A, Böhme W, Schmitt W. Application of micromechanical models to the analysis of ductile fracture under dynamic loading. In: Erdogan F, Hartranft RJ, editors. *Fracture Mechanics, 25th Vol: American Society for Testing and Materials*; 1994. p. 343-357.
- [22] Heerens J, Schödel M. On the determination of crack tip opening angle, CTOA, using light microscopy and  $\delta_5$  measurement technique. *Eng Fract Mech*. 2003;70(3-4):417-426.
- [23] Morgener TF, Starink MJ, Sinclair I. Evolution of voids during ductile crack propagation in an aluminium alloy sheet toughness test studied by synchrotron radiation computed tomography. *Acta Materialia*. 2008;56(8):1671-1679.
- [24] Pardo T, Hutchinson JW. Micromechanics-based model for trends in toughness of ductile metals. *Acta Mater*. 2003;51:133-148.
- [25] Steglich D, Brocks W, Heerens J, Pardo T. Anisotropic ductile fracture of Al 2024 alloys. *Eng Fract Mech*. 2008;75:3692-3706.

## Tables

Table 1: Composition of Al 2198 T8 by chemical analysis

Element	Cu	Li	Mg	Ag	Zr	Fe	Zn	Si	Al
wt%	3.1	1.0	0.3	0.06	0.11	0.046	0.014	0.033	93

Table 2: Mechanical properties of Al 2198 T8

Tensile direction	Yield stress [MPa]	Tensile strength [MPa]	R-value [.]	Fracture strain [.]
L	469	510	0.7	0.14
T	452	498	1.5	0.13
D	394	436	2.0	0.16

Table 3: Results of the microstructural characterisation

Cross section	Particle surface fraction $A_p$ [%]	Mean particle diameter [ $\mu\text{m}$ ]	Mean nearest neighbour distance [ $\mu\text{m}$ ]	Mean shape factor $S_f$ [.]
LT	0.27	1.8	12	0.8
LS	0.24	1.8	14	0.8
TS	0.23	1.7	14	0.8

Table 4: Model parameters used in the simulations

Parameter	Value	Parameter	Value
$E$ [MPa]	73000	$\nu$	0.3
$\alpha$	0.5	$b_1$	16
$a$	16	$b_2$	16
$c_1^{(1)}$	1.010	$c_1^{(2)}$	1.128
$c_2^{(1)}$	1.073	$c_2^{(2)}$	0.810
$c_3^{(1)}$	1.005	$c_3^{(2)}$	0.945
$c_4^{(1)}$	1.243	$c_4^{(2)}$	1.003
$c_5^{(1)}$	1.000	$c_5^{(2)}$	1.000
$c_6^{(1)}$	1.000	$c_6^{(2)}$	1.000
$f_0$	0.0027		
$\varepsilon_0$	0.1	$A$	0.02
$f_c$	0.009	$K$	3
$q_1$	1.4	$q_2$	1.1

**Figures**

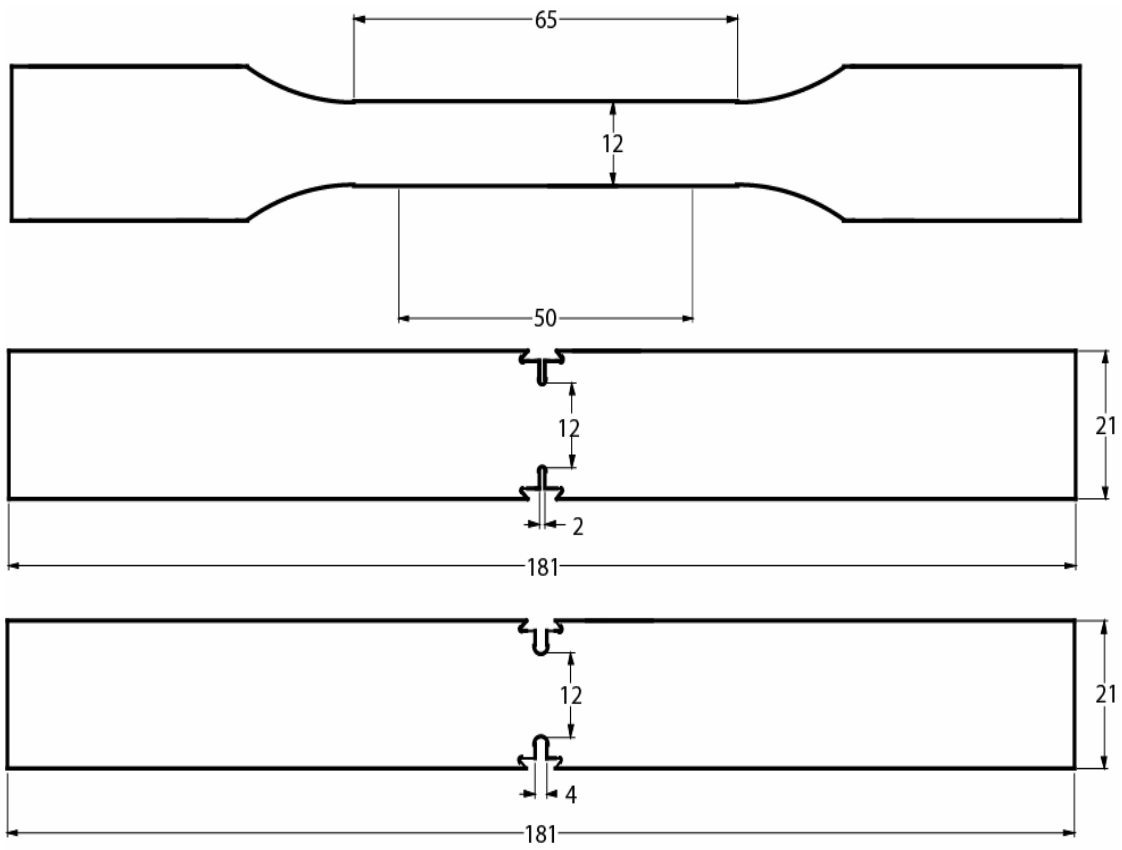


Figure 1: specimen geometries used in the tests (thickness is 3.1 mm)

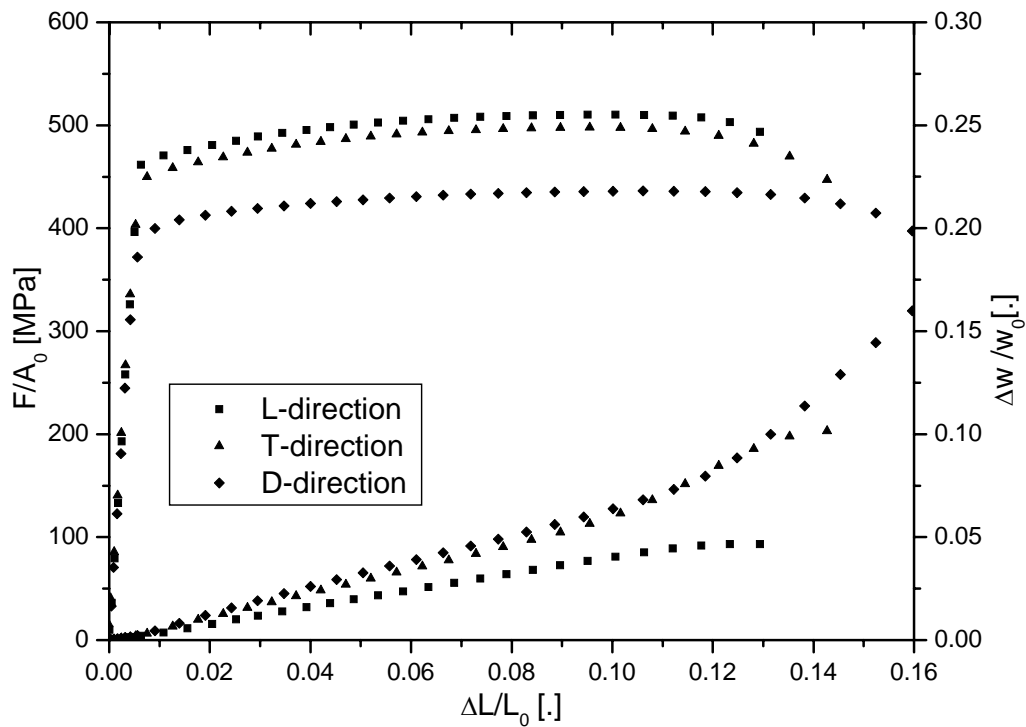


Figure 2: Results of the smooth tensile tests in terms of engineering stresses – elongation and reduction of width – elongation

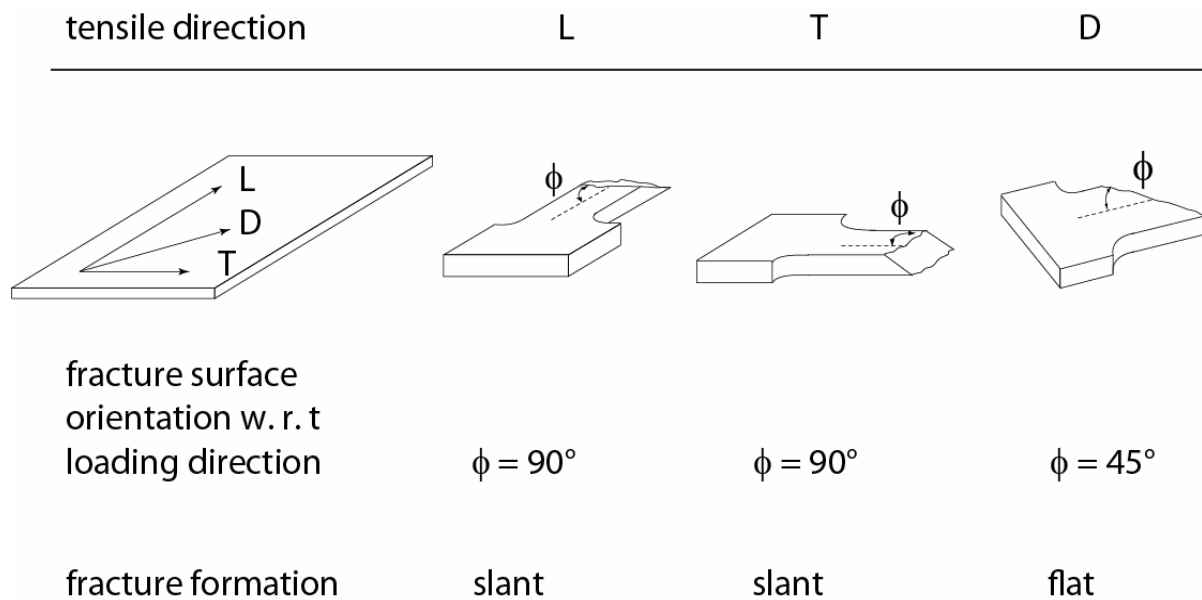


Figure 3: Macroscopic crack formation during the tensile tests on smooth bars

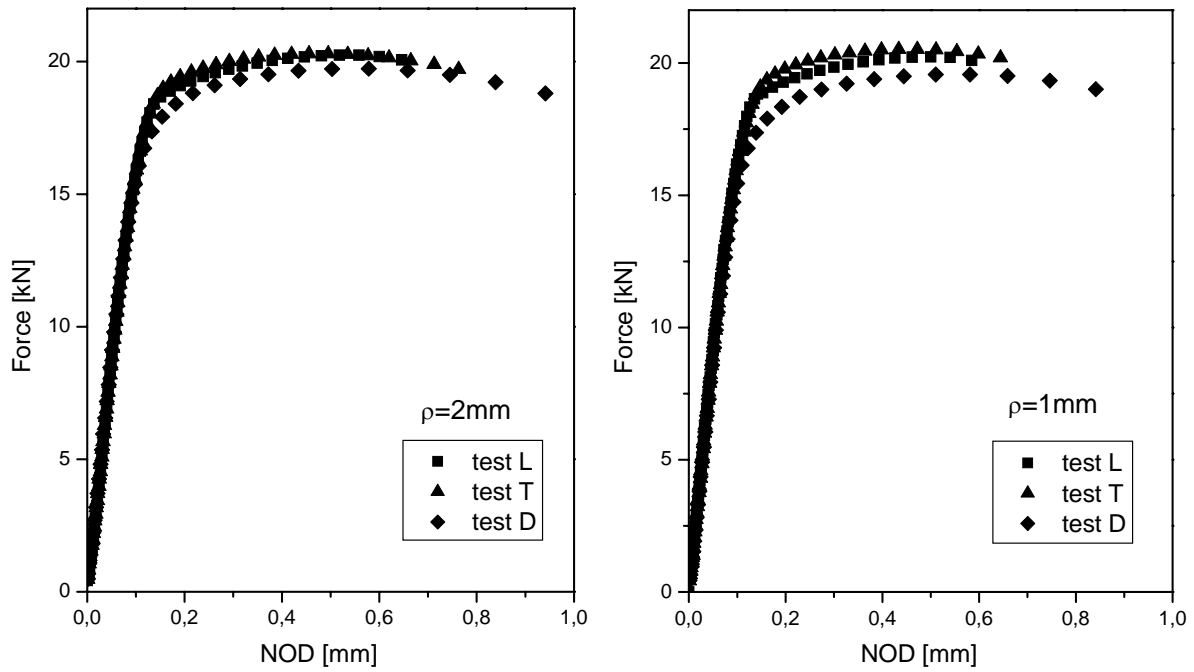


Figure 4: Force – deformation behaviour of the two different notched specimen types,  $\rho=2$  mm and 1 mm, respectively

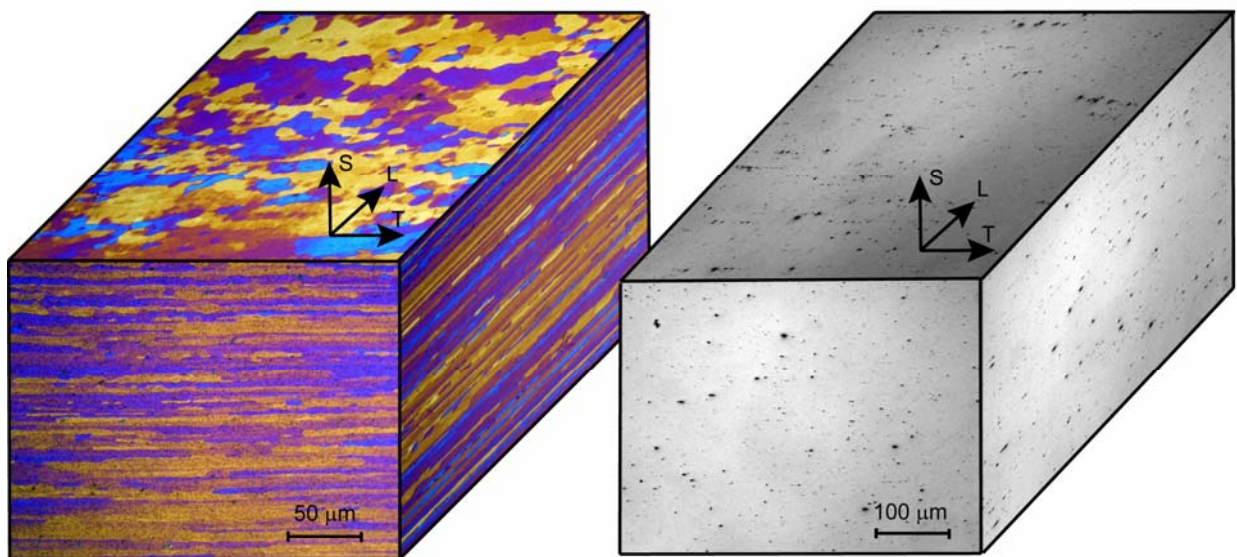


Figure 5: Microstructure of Al 2198 sheet material: grain structure (left) and particle morphology (right)

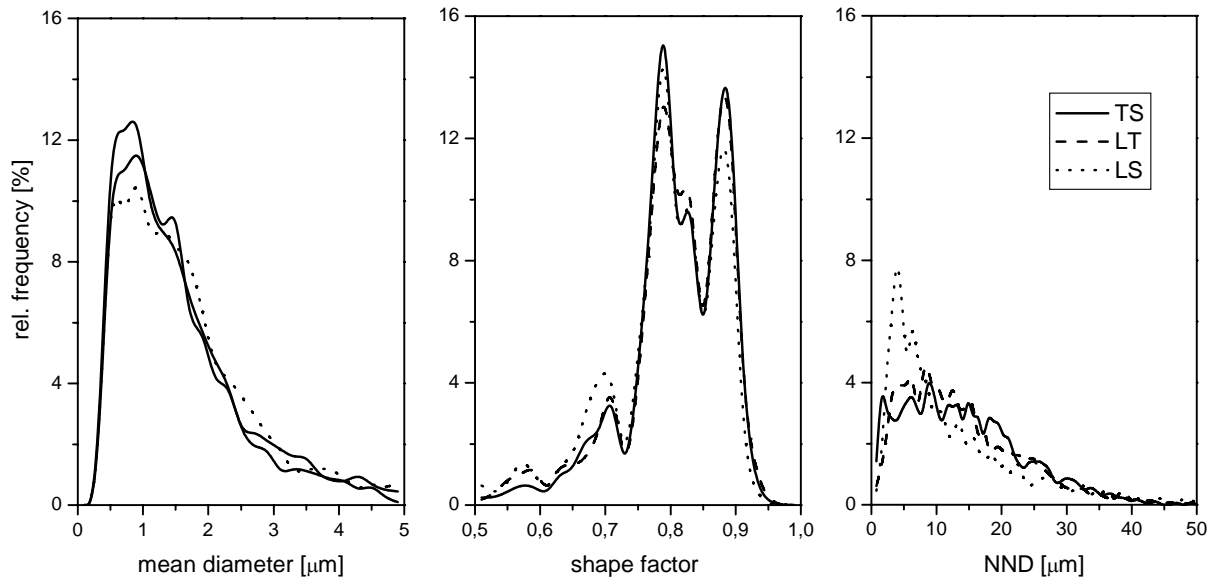


Figure 6: Distributions of microstructural quantities for different cross sections (NND: nearest neighbour distance)

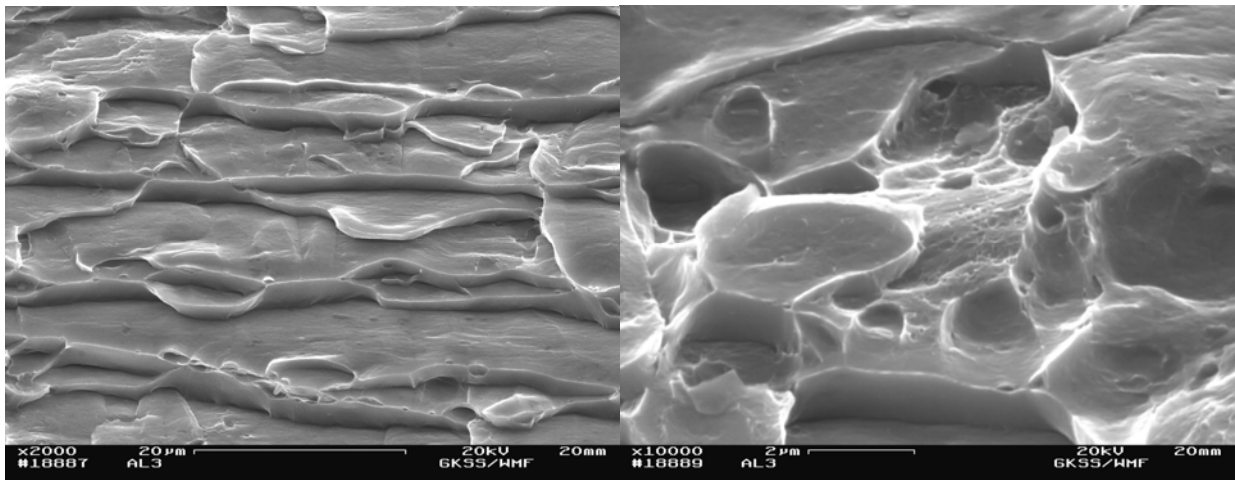


Figure 7: Micrograph of the fracture surface of the smooth tensile bar loaded in L-orientation showing large areas of inter-crystalline shear fracture and small regions of dimples in region of the the slanted surface

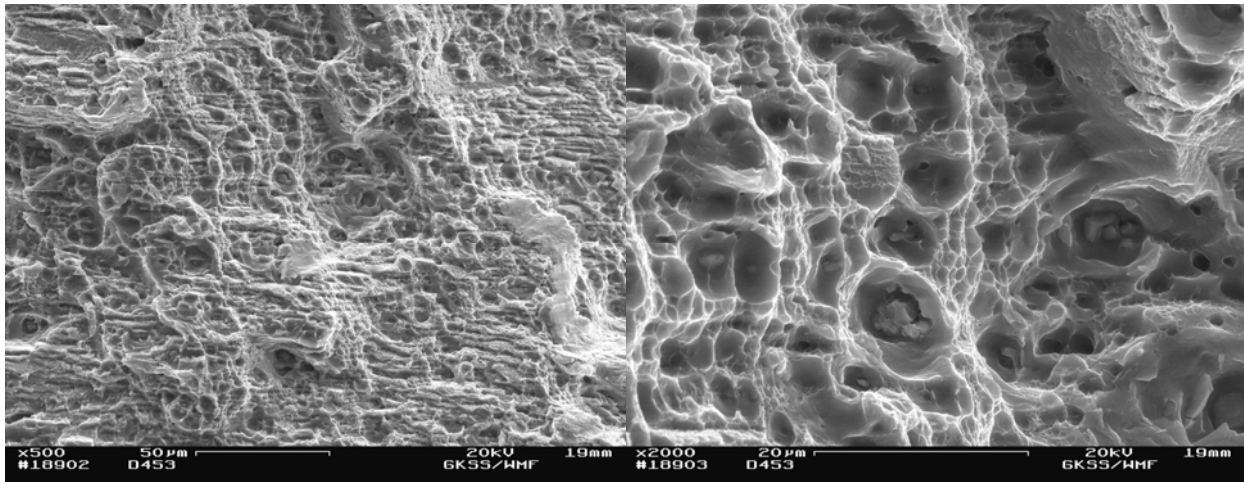


Figure 8: Micrograph of the fracture surface of the smooth tensile bar loaded in D-orientation showing dimples with second phase particles

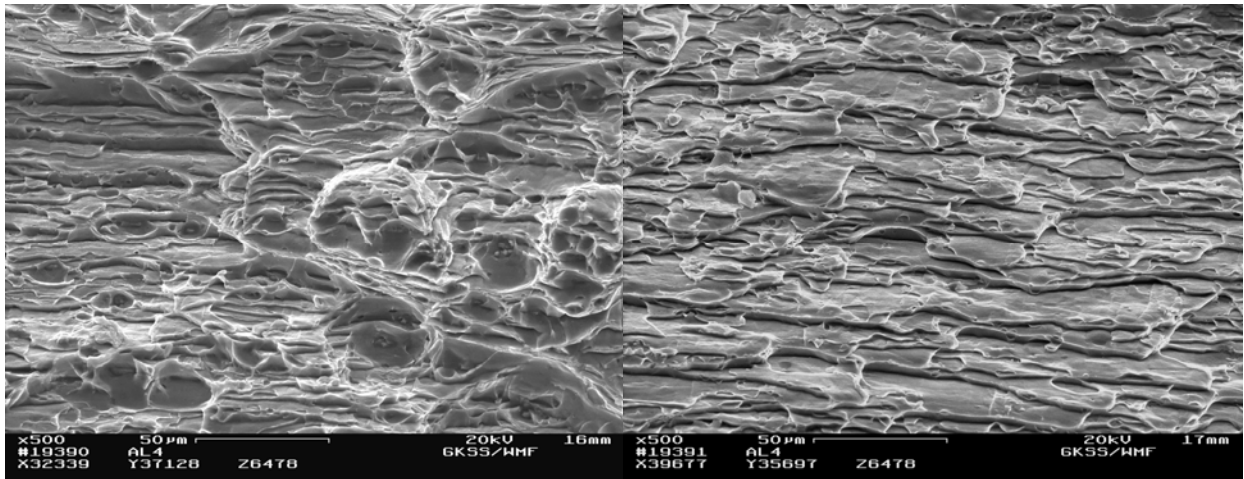


Figure 9: U-notched specimen fracture surface ( $\rho=1$  mm): ductile failure mechanism at the notch root (left), inter-crystalline shear failure in the specimen's centre

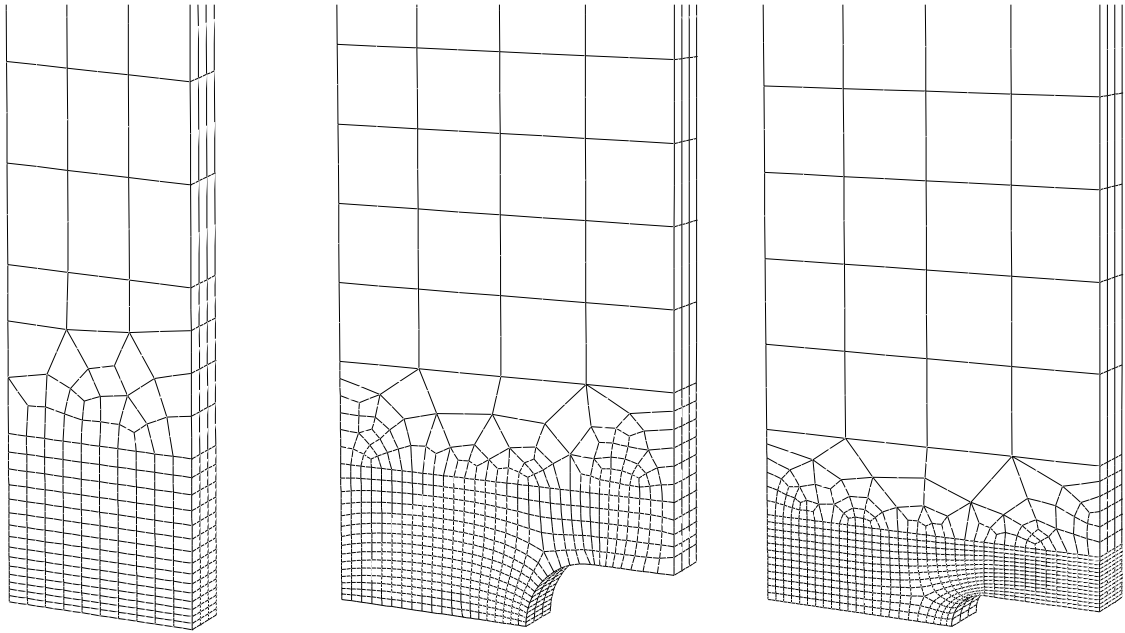


Figure 10: Finite element meshes (smooth bar, notched bars  $\rho=2$  mm and  $\rho=1$  mm) used for the simulations exploiting threefold symmetry

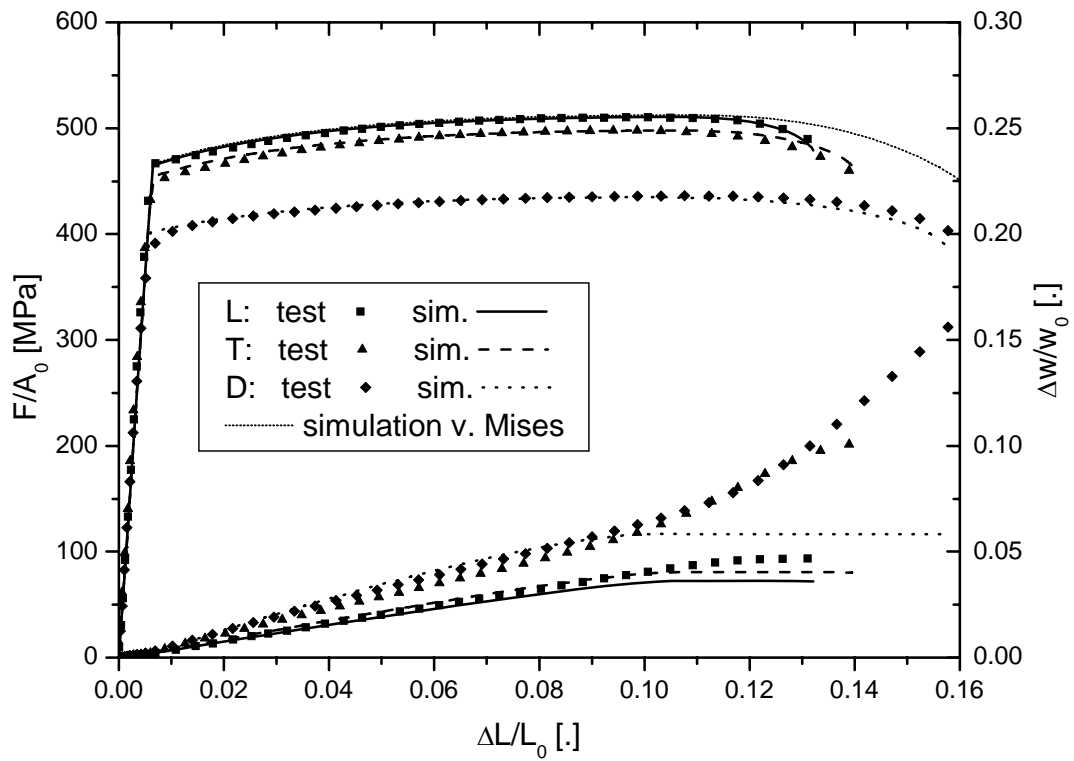


Figure 11: smooth tensile tests – results of the parameter fit

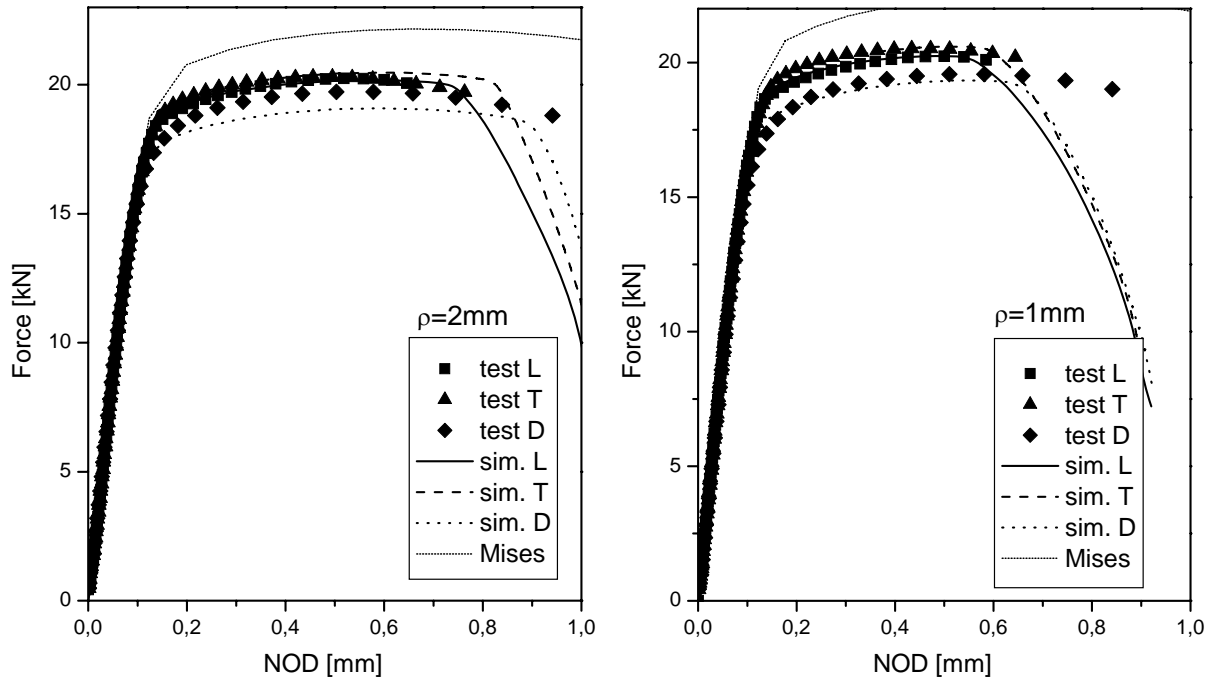


Figure 12: simulations of the force – NOD behaviour of the notched specimens in experiment and simulation

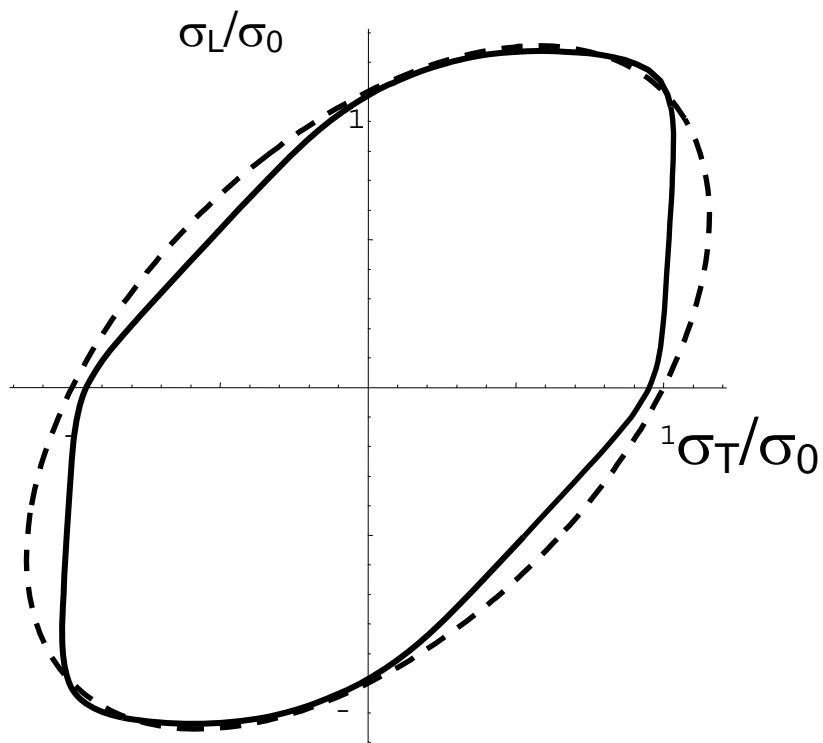


Figure 13: graphical representation of the Bron-yield surface (solid line) in the space of the in-plane stresses in comparison to the von Mises ellipse (dashed line).